



One-step synthesis of ultrafine MoNiS and MoCoS monolayers as high-performance catalysts for hydrodesulfurization and hydrodenitrogenation

Kun Guo^{a,b}, Yi Ding^c, Zhixin Yu^{a,b,*}



^a Department of Energy and Petroleum Engineering, University of Stavanger, 4036 Stavanger, Norway

^b The National IOR Centre of Norway, University of Stavanger, 4036 Stavanger, Norway

^c Institute for New Energy Materials & Low-Carbon Technologies, School of Materials Science and Engineering, Tianjin University of Technology, Tianjin 300384, China

ARTICLE INFO

Keywords:
 One-step
 Monolayers
 Ultrafine
 Molybdenum disulfide
 Hydrodesulfurization
 Hydrodenitrogenation

ABSTRACT

A one-step facile strategy is developed to prepare highly disordered MoS_2 -based monolayers via the thermal organometallic decomposition in the presence of elemental sulfur and oleylamine. Characterizations including TEM, SEM, XRD, Raman spectroscopy, XPS, and nitrogen adsorption–desorption confirm the monolayer structure of the MoS_2 -based sulfides with similar ultrasmall lateral sizes of 4.2–4.6 nm and the successful doping of Ni and Co atoms in MoNiS and MoCoS. Due to the abundant active sites enabled by the ultrafine monolayer structure, these sulfides exhibit significantly improved activity in the hydrodesulfurization (HDS) of thiophene and hydrodenitrogenation (HDN) of pyridine compared to the commercial multilayer MoS_2 . Rational comparison of these catalysts justified by almost the same size, morphology, specific surface area confirms the superior promoting roles of Co for the HDS while Ni for the HDN, and further demonstrates that pyridine is a competitive inhibitor for thiophene in binding to the active sites of the catalysts. Moreover, excellent reusability for five consecutive cycles in the HDS and HDN is exhibited by MoCoS and MoNiS, respectively, which is attributed to their well-retained monolayer structure during the tests. This study highlights the significance of advanced synthetic strategy for improving the catalytic performance of Mo-based sulfides as industrial HDS and HDN catalysts.

1. Introduction

Emission of sulfur dioxide (SO_2) and nitrogen oxides (NO_x), due to the combustion of petroleum-derived fuels such as gasoline and diesel, has been recognized as a major cause of the notorious acid rain and air pollution. To protect the environment, many countries have issued increasingly stringent legislations to reduce the contents of sulfur and nitrogen in transportation fuels to a very low level [1–5]. These regulations are thus dictating high requirements on the oil refineries, where the crude oils are upgraded in a series of hydrotreating processes including hydrodesulfurization (HDS) and hydrodenitrogenation (HDN). Either the severity of the reaction conditions or the improvement of employed catalysts should be considered for producing ultra-clean fuels with S and N contents meeting the standards.

Mo(W) sulfides promoted by Co(Ni) and supported on $\gamma\text{-Al}_2\text{O}_3$ have been used as the industrial HDS and HDN catalysts for several decades. It is well documented that the key active species in the catalysts consist of Mo(W), Co(Ni) and S atoms on the edges of the lamellar Mo(W) sulfides [6–10]. Conventionally, the Mo(W)Co(Ni)S are prepared by the

two-step processes of precipitation and post-sulfidation, which could generate catalysts with low density of active sites and unfavorable nanostructure. Besides, the sulfidation process is often inadequate, resulting in a co-existence of oxides and sulfides in the catalysts. To upgrade the classic Mo(W)Co(Ni)S catalysts, rational design and controlled synthesis to create high density and availability of the active edge sites are necessary. For instance, Tang's group [11] reported that by introducing Mo and Co species into the meso- and micropores of mordenite nanofibers, a much higher activity and longer catalyst life in the HDS of 4,6-dimethylbenzothiophene were achieved by the CoMo/mordenite catalyst compared with a conventional CoMo/ $\gamma\text{-Al}_2\text{O}_3$.

One-step synthetic strategy, using either the decomposition of thiosalts or the direct sulfidation of metal precursors, has been adopted to prepare layered Mo-based materials not only as catalysts for HDS and HDN but also as indispensable materials in distinct applications [12–18]. Yan et al. [19] obtained ultrathin MoS_2 nanoplates with rich active sites by the direct solvothermal decomposition of $(\text{NH}_4)_2\text{MoS}_4$. Afanasiev et al. [20] prepared highly dispersed MoS_2 by reducing $(\text{NH}_4)_2\text{MoS}_4$ in the presence of a surfactant. Direct sulfidation of

* Corresponding author at: Department of Energy and Petroleum Engineering, University of Stavanger, 4036 Stavanger, Norway.

E-mail address: zhixin.yu@uis.no (Z. Yu).

ammonium molybdate with elemental S was reported to synthesize MoS₂ nanoflowers constructed by single-layered or few-layered MoS₂ nanosheets [21,22]. By one-pot reaction of Mo(CO)₆ and S in xylene solvent, Cho's group [23] prepared MoS₂ nanoplates consisting of disordered graphene-like sheets. It has also been proven that Co(Ni) precursors can be readily introduced in the synthesis to obtain MoS₂ promoted with Co(Ni) [24,25]. These studies and many more have demonstrated that the one-step methods offer high feasibility to tailor-make and fine-tune the nanostructure and morphology of Mo sulfides. Furthermore, the resulting sulfides through one-step synthesis normally end up being unsupported, which endows them with abundant and stable active sites. The unsupported Mo(W)Co(Ni)S catalysts have also been demonstrated to perform better in the HDS and HDN compared to the traditional supported ones [26–29]. Therefore, one-step synthesis of unsupported Mo(W)Co(Ni)S catalysts with well-defined structure holds great potential for enhancing their catalytic performance in the HDS and HDN reactions.

Analogous to graphene and graphite, the properties of MoS₂ change dramatically when the stacking layers are exfoliated into monolayers, especially in catalytic applications [22,30–32]. Distorted MoS₂ monolayers often contain a high density of dislocations, which creates abundant defect sites that are catalytically active. In addition, the reduction of the lateral size of MoS₂ monolayers to nanoscale can turn the inactive basal plane sites into active edge sites. Nevertheless, the facile preparation of MoS₂ monolayers with ultrafine lateral sizes remains challenging and further efforts are necessary.

Herein, a one-step facile synthetic method, based on the thermal decomposition of organometallic precursors and sulfidation with elemental S in oleylamine solvent, is developed to prepare highly dispersed, unsupported MoS₂ monolayers doped with Ni or Co (designated as MoNiS and MoCoS). Detailed characterization techniques are utilized to acquire compositional and structural information of the resulting MoS₂, MoNiS and MoCoS. Their catalytic performance in both individual and simultaneous HDS and HDN is studied using a batch reactor with thiophene and pyridine as the S- and N-containing model compounds, and compared with a commercial multilayer MoS₂ (designated as c-MoS₂) catalyst. Difference of the Co and Ni as promoting cations in HDS and HDN is examined. The competing adsorption of thiophene and pyridine to the active sites is studied when comparing the results from simultaneous HDS and HDN to the individual reaction. The reusability of MoNiS and MoCoS catalysts is also tested in consecutive reactions. This study highlights the importance of advanced synthetic strategy for enhancing the performance of nanostructured Mo-based sulfides as industrial HDS and HDN catalysts.

2. Experimental

2.1. Chemicals

All chemicals were purchased unless otherwise indicated and used as received without further treatment. Chemicals including molybdenum hexacarbonyl (Mo(CO)₆, ≥99.9%), nickel(II) acetylacetone (Ni(acac)₂, 95%), cobalt(III) acetylacetone (Co(acac)₃, 98%), sulfur (99.998%), oleylamine (OAm, technical grade, 70%), molybdenum(IV) disulfide nanopowder (MoS₂, average particle size of 90 nm, 99%), pyridine (anhydrous, 99.8%), 1,2,3,4-tetrahydronaphthalene (tetralin, 99%), and naphthalene (≥99%) were purchased from Sigma-Aldrich. Thiophene (≥99%), hexane (≥99%), ethanol (96 vol. %) and toluene (≥99.5%) were ordered from VWR International AS.

2.2. Synthesis of sulfide catalysts

The sulfide catalysts were prepared via the modified heat up method [33,34]. Fig. 1 illustrates the one-step synthetic procedure. For the synthesis of MoNiS, a 250 mL round bottom three-neck flask containing

20 mL of OAm, 1.6 mmol of Mo(CO)₆, 0.4 mmol of Ni(acac)₂ and 4.0 mmol of sulfur was heated up to 80 °C using a heating mantle (Glas-Col, LLC). The flask was connected with a nitrogen gas inlet and a reflux condenser attached with a bubbler. After purging the flask with nitrogen for at least 30 min, temperature of the heating mantle was elevated to 300 °C. The reaction was held for 1 h and the flask was cooled down naturally. The reaction medium was constantly stirred with a magnetic stir bar at 1000 rpm. Afterwards, a mixture of hexane and ethanol (v/v = 1/3) was added to extract the products, and centrifugation was conducted to separate them at 9000 rpm for 5 min. This process was repeated at least 3 times to remove residual surfactants and impurities. The final powder was collected by drying the sample in an electronic oven at 60 °C overnight. MoCoS was prepared by replacing the same amount of Ni(acac)₂ by Co(acac)₃, whereas MoS₂ was prepared by using 2.0 mmol of Mo(CO)₆ as the only precursor.

2.3. Catalyst characterization

The microstructures and morphology of sulfide samples were characterized by transmission electron microscopy (TEM, JEOL JEM-2100F, 200 kV) and scanning electron microscopy (SEM, FEI Helios NanoLab 460HP, 10 kV). Elemental mapping of the sulfide samples was carried out using an energy dispersive X-ray (EDX) analyzer attached to SEM. For the specimen preparation, one droplet of the sulfide suspension was dropped onto a copper grid coated with carbon film (400 mesh, TAAB) and dried in air.

X-ray diffraction (XRD) was performed to obtain the crystallographic information of the samples. The powder diffraction patterns were recorded on a Bruker-AXS Microdiffractometer (D8 ADVANCE) using Cu K α radiation source ($\lambda = 1.5406 \text{ \AA}$, 40 kV and 40 mA). Scanning angles for all samples were set in the 2 θ range of 10–90° with a step interval of 2.0°/min. Peaks were indexed according to the database established by Joint Committee on Powder Diffraction Standards (JCPDS).

The Raman spectrum was obtained using JOBIN YVON HR800 laser confocal micro-Raman spectroscopy equipped with an optical microscope, a CCD camera and an argon ion laser source. The laser provided 50 mW power at 514.5 nm for the exciting line.

X-ray photoelectron spectroscopy (XPS) analysis was performed on the ESCALAB 250Xi (Thermo Scientific) XPS system utilizing a monochromatic Al K α source (1486.6 eV). High-resolution spectra were obtained at a pass energy of 30.0 eV, a step size of 0.1 eV, and a dwell time of 500 ms per step. All spectra were referenced to the C 1s peak (284.8 eV).

Nitrogen adsorption–desorption measurements were conducted at the liquid nitrogen temperature of 77 K on a Micromeritics TriStar II surface area and porosity analyzer after degassing under vacuum at 100 °C for 8 h using a sample degas system (Micromeritics VacPrep 061). Specific surface area (SSA) was calculated using the Brunauer–Emmett–Teller (BET) method. Pore size distribution was determined by the Barrett–Joyner–Halenda (BJH) method based on the desorption branch of the isotherm.

2.4. HDS of thiophene

HDS reaction of thiophene was performed in a 4564 Parr Mini Bench Top Reactor with a volume capacity of 160 mL. The key components of this reactor vessel were made of Type 316 stainless steel. Blank tests were conducted to exclude the catalytic effect of the reactor itself. Typically, a 40 mL liquid mixture composed of thiophene as the sulfur-containing compound, tetralin as the hydrogen donor and hexane as the solvent in a volume ratio of 1:9:10, together with 100 mg of catalysts were loaded into the reactor. After being tightly sealed, the reactor was sonicated in an ultrasound bath for 10 min to disperse the catalysts. Hydrogen (purity 5.0, Praxair Norge AS) was used to purge the reactor for 30 min and then pressurize it to 11 bar. Our previous

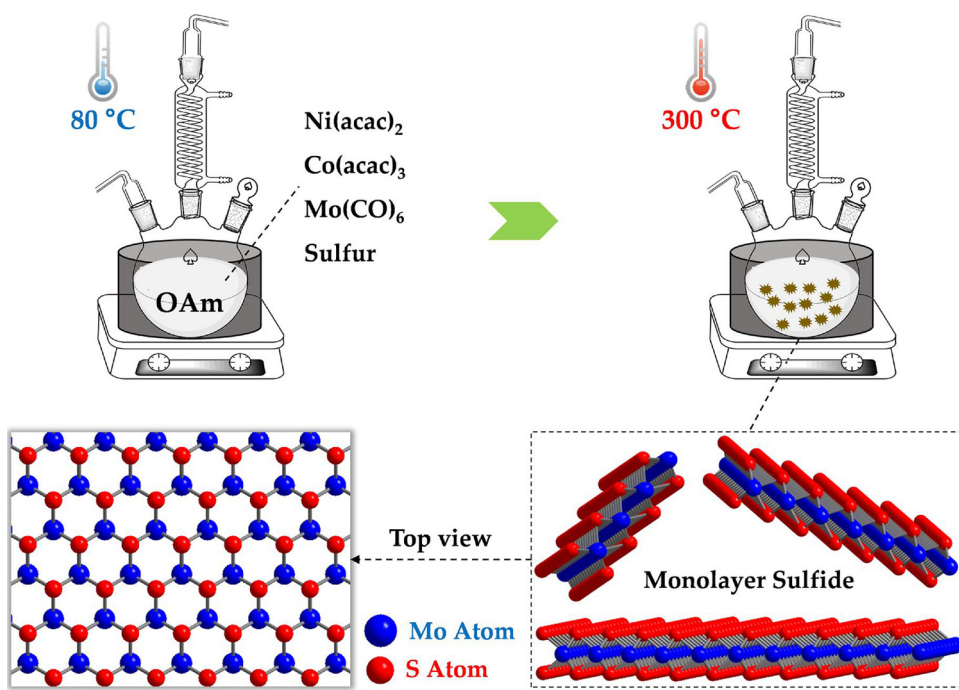


Fig. 1. Schematic illustration of the one-step synthesis procedure to prepare MoS_2 , MoNiS and MoCoS catalysts.

work has demonstrated that both tetralin and hydrogen serve as effective hydrogen donor in the HDS reaction [35]. Afterwards, the reactor was heated up from room temperature to 300 °C and the reaction system was held for different periods. During the whole reaction period, the stirring torque was maintained at half of the full power. After cooling down naturally, the reactor was depressurized to atmosphere pressure. Measurement of the thiophene content before and after the reaction was carried out on an Agilent 7820 Gas Chromatograph (GC) equipped with a J&W HP-5 column (length 30 m, diameter 0.25 mm, thickness 1.0 μm) and a flame ionization detector (FID). Fig. S1 shows the GC spectra of several standard reference compounds and the initial reactant solution. Naphthalene is found as a new product after the HDS, which shall be attributed to the dehydrogenation of tetralin [35]. In each analysis, 600 μL sample liquid from the reactor was diluted with 600 μL toluene solvent, and this mixture was utilized to measure the thiophene concentration. Each sample test was repeated three times on the GC and the average value was taken as the thiophene concentration. Calculation of the thiophene conversion was expressed by the equation as below

$$\Delta C = \frac{C_0 - C_1}{C_0} \times 100\% \quad (1)$$

where ΔC is the thiophene conversion ratio; C_0 and C_1 are the thiophene concentration before and after the HDS reaction, respectively. Assuming a pseudo-first-order reaction for the HDS of thiophene, the reaction rate constant was calculated by the following equation

$$\ln(1 - \Delta C) = -k \cdot t \quad (2)$$

where k is the pseudo-first-order rate constant and t is the reaction time.

2.5. HDN of pyridine

HDN reaction of pyridine was conducted similarly as the HDS reaction except that a 40 mL liquid mixture composed of pyridine, tetralin and hexane in the volume ratio of 0.4:9:10.6 was used as the initial solution. Pyridine conversion and reaction rate constant were calculated with the same methods as above.

2.6. Simultaneous HDS and HDN

Simultaneous HDS and HDN reactions of thiophene and pyridine were also conducted similarly as the HDS reaction except that a 40 mL liquid mixture composed of thiophene, pyridine, tetralin and hexane in the volume ratio of 0.5:0.2:9:10.3 was used as the initial solution. Thiophene and pyridine conversions were calculated with the same methods as above.

3. Results and discussion

3.1. Material characterization

Thermal decomposition of organometallic precursors has previously been used to prepare monodispersed metal, oxide and phosphide nanoparticles [36,37]. In this study, a similar synthetic protocol is utilized to prepare highly dispersed MoS_2 monolayers doped with Ni or Co. Fig. 1 illustrates the synthetic procedure and monolayer structure together with the atomic arrangements of MoS_2 , MoNiS and MoCoS . In the synthesis of MoS_2 , a homogeneous solution containing $\text{Mo}(\text{CO})_6$ and elemental sulfur dissolved in OAm is obtained first at 80 °C and then heated up to 300 °C. At this high temperature, $\text{Mo}(\text{CO})_6$ decomposes and reacts with sulfur to form MoS_2 . In addition, the solvent OAm also serves as a surfactant. The OAm molecules bind to the metal surface through the strong coordination between nitrogen and metal atoms. Once this coordination overwhelms the Van der Waals interactions, which governs the stacking of layer structure along the c -axis, monolayer MoS_2 is formed with restrained growth only along the a - and b -axis. This in-plane growth is also affected by the binding of OAm molecules, thus controlling the lateral sizes of MoS_2 monolayers. By adding the $\text{Ni}(\text{acac})_2$ or $\text{Co}(\text{acac})_3$ precursors, MoNiS and MoCoS are prepared with Ni and Co atoms substituting the Mo randomly in the hexagonal structural units of MoS_2 . The molar ratio of Ni or Co to Mo is set to 1:4. In addition, commercial MoS_2 nanopowder with an average particle size of 90 nm is used as a reference.

The morphology of the as-prepared MoS_2 , MoNiS and MoCoS is analyzed by TEM characterization. Fig. 2a–c shows the representative high-magnification TEM images of MoS_2 , MoNiS and MoCoS ,

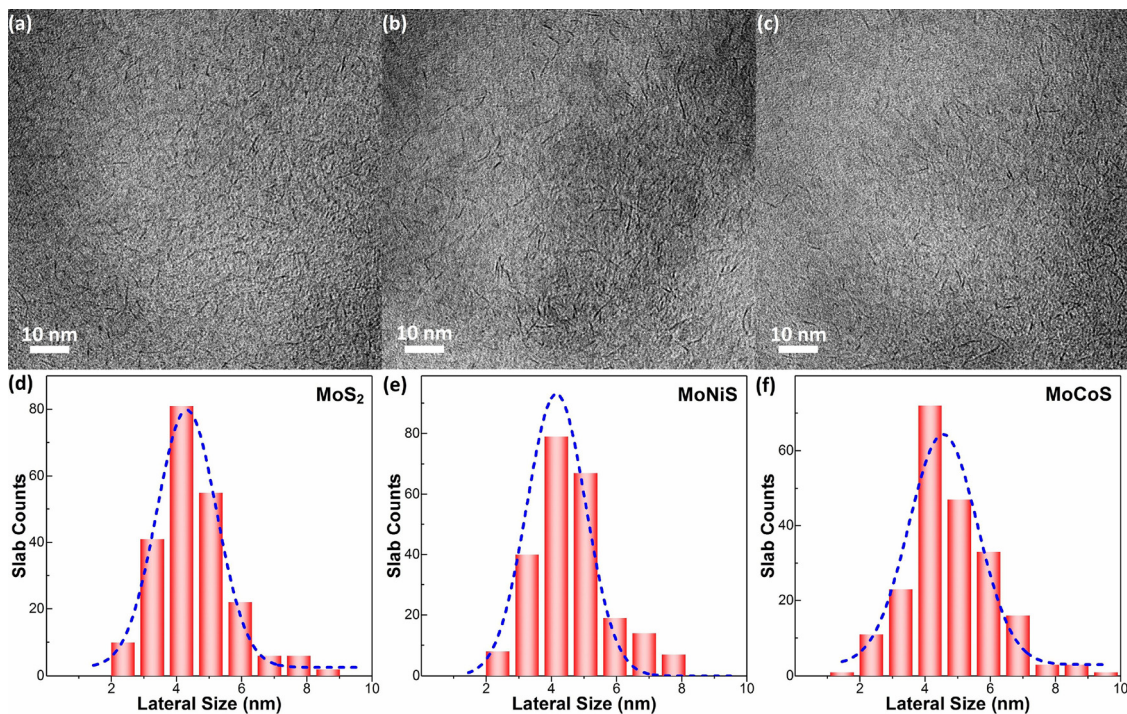


Fig. 2. TEM images and corresponding lateral size distribution curves with Gaussian fits of MoS₂ (a, d), MoNiS (b, e) and MoCoS (c, f).

respectively. The monolayer structure in random orientation can be clearly observed from the side view for all the MoS₂-based sulfides. The formation of these unstacked monolayers should be attributed to the OAm as a strong capping agent to avoid the Van der Waals interactions. A portion of the monolayers is also found distorted, indicating a defect-rich structure of these sulfides. Fig. 2d–f presents the lateral size distributions of the MoS₂, MoNiS and MoCoS monolayers, respectively. The average lateral sizes are determined using Gaussian fits based on the statistic count of at least 200 side-viewed monolayers. It is found that the MoS₂, MoNiS and MoCoS have very close average lateral sizes of 4.3 ± 0.1 , 4.2 ± 0.1 and 4.5 ± 0.2 nm. The ultrasmall lateral sizes indicate the high content of active edge sites in these sulfides, which is desirable for the catalytic applications.

Fig. 3 presents the low-magnification SEM images and corresponding elemental mapping of MoNiS and MoCoS. It is revealed that both MoNiS (Fig. 3a) and MoCoS (Fig. 3b) are composed of large

aggregates of the monolayers, resulting in an irregular surface. The corresponding elemental mapping confirms the uniform distribution of Mo (Fig. 3c), S (Fig. 3d) and Ni (Fig. 3e) for MoNiS, and Mo (Fig. 3f), S (Fig. 3g) and Co (Fig. 3h) for MoCoS, suggesting that the Ni and Co atoms are homogeneously distributed in the MoS₂ monolayers. Similar structural information can be acquired from the SEM image and elemental mapping of MoS₂ (Fig. S2). The EDX spectra of MoS₂, MoNiS and MoCoS is shown in Fig. S3 and the corresponding atomic percentage is listed in Table S1. For Ni- or Co-doped sulfides, the atomic ratio of Mo/S is close to 0.4:1, consistent with the stoichiometric ratio. Besides, the approximate atomic ratio of Ni/Mo and Co/Mo are largely in accordance with their precursor ratios of 1:4. The nitrogen adsorption–desorption isotherms and BJH pore size distribution curves of MoS₂, MoNiS and MoCoS together with their BET SSAs are presented in Figs. S4 and S5. The ill-defined pore structure of these sulfides is confirmed by the shape of the isotherms and the wide distribution of pore

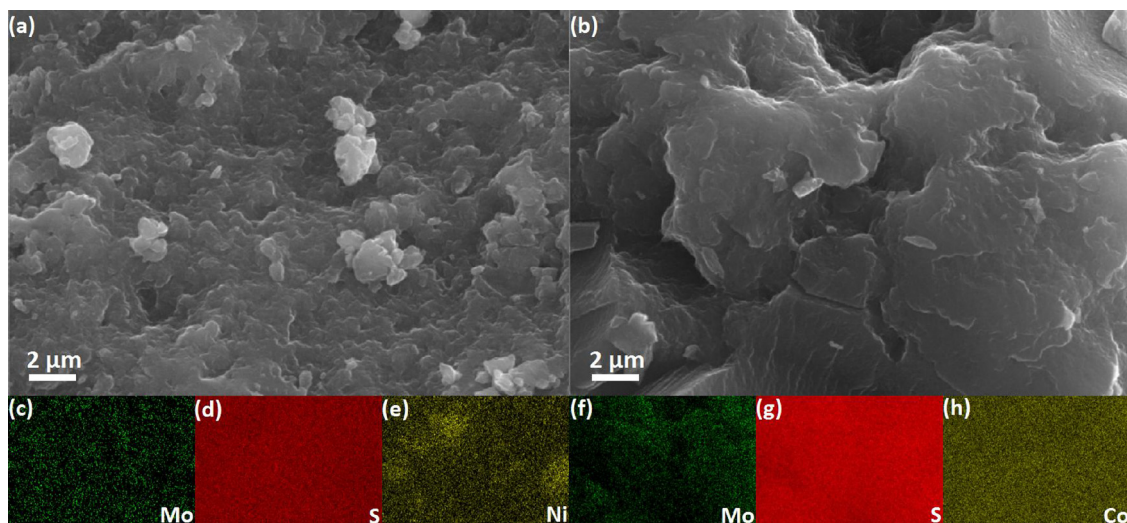


Fig. 3. SEM images of MoNiS (a) and MoCoS (b), and their corresponding elemental mapping of Mo (c, f), S (d, g), Ni (e), and Co (h).

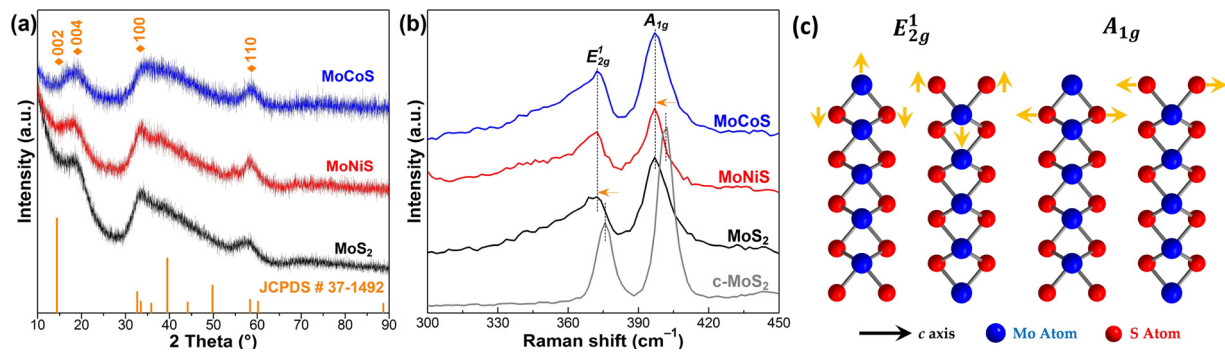


Fig. 4. XRD patterns (a) and Raman spectra (b) of c-MoS₂, MoS₂, MoNiS, and MoCoS. (c) Schematic illustration of the E_{2g}^1 and A_{1g} vibration modes of MoS₂.

sizes. Such pores should be accounted to the gap space between the randomly stacked monolayers instead of built-in formation. These sulfides possess a very close SSA of around $45\text{ m}^2/\text{g}$, allowing a fair comparison of their catalytic activity.

XRD characterization is carried out to examine the composition and crystal phase of the MoS₂, MoNiS and MoCoS. Fig. 4a shows that the three sulfides display almost the same diffraction pattern and the identified diffraction peaks can be indexed to the hexagonal 2H-MoS₂ phase (JCPDS card No. 37-1492). The weak intensity of peaks at 32.7° and 58.3° , corresponding to the (100) and (110) in-plane diffraction, indicates the poor crystallinity and small crystalline domains of these sulfides. The absence of the (002) characteristic peak at 14.3° suggests no evident stacking of the MoS₂ monolayers along the c-axis. The weak peak appearing at 18.5° should be ascribed to the shift of (004) peak originally located at 29.0° of the 2H-MoS₂ phase [21,23]. According to the Bragg's law, this shift can be explained by the largely extended interplanar spacing along the c-axis. These results accord well with that observed from the TEM characterization. In contrast, the XRD pattern of the c-MoS₂ nanopowder in Fig. S6 indicates its highly crystalline and multilayer nature.

Raman spectroscopy is employed to obtain the structural information of all the MoS₂-based sulfides. Fig. 4b shows that two distinct peaks at 373.5 and 397.2 cm^{-1} , corresponding to the in-plane E_{2g}^1 and out-of-plane A_{1g} vibration modes, can be observed for MoS₂, MoNiS and MoCoS, indicating the same MoS₂-based layer structure and the doping of Ni and Co largely located at the layer edge sites. As illustrated in Fig. 4c, the E_{2g}^1 is attributed to the opposite vibration of S atoms relative to the Mo atoms in between, whereas the A_{1g} mode results from the vibration of only S atoms in the opposite directions. Previous studies have demonstrated that along with the increase of MoS₂ layer number, the E_{2g}^1 mode undergoes a red shift while the A_{1g} mode undergoes a blue shift [24,31,38]. Raman spectra of the multilayer c-MoS₂ is also analyzed as a reference. The A_{1g} peak of c-MoS₂ appears at 401.7 cm^{-1} , indicating that the A_{1g} peak at 397.2 cm^{-1} of MoS₂, MoNiS and MoCoS is blue shifted, which accords with their monolayer structure. However, their E_{2g}^1 peak at 373.5 cm^{-1} is not red shifted compared to the E_{2g}^1 peak at 375.9 cm^{-1} of the multilayer c-MoS₂, which should be ascribed to the disturbance of distorted, defect-rich layer structure and ultrafine lateral sizes of the sulfides [17–19,31,39]. The results from Raman study are consistent with the TEM and XRD observations.

XPS measurements are conducted to investigate the chemical composition and elemental states of the MoS₂, MoNiS and MoCoS. Fig. 5 presents the high-resolution XPS spectra of Mo 3d, S 2p and Ni 2p for the MoNiS, and Mo 3d, S 2p and Co 2p for the MoCoS. The XPS spectra of Mo 3d and S 2p for the MoS₂ is shown in Fig. S7. Similar XPS spectra of both the Mo 3d and S 2p regions is observed among these sulfides. Their specific peak positions are listed in Table S2. In the XPS spectra of the Mo 3d region, two major peaks at binding energy of 229.1 and 232.4 eV are assigned to the Mo^{4+} $3d_{5/2}$ and Mo^{4+} $3d_{3/2}$ in MoS₂, indicating the dominance of Mo^{4+} in MoNiS and MoCoS. A small XPS peak at 235.8 eV can be ascribed to the Mo^{6+} $3d_{5/2}$ of MoO₃, which

may be ascribed to the partial oxidation of MoS₂ when exposed in air. In addition to the Mo 3d signals, a peak at 226.3 eV belonging to the S 2s orbital is observed. The XPS spectra of S 2p region can be resolved into two spin-orbit doublets (S $2p_{1/2}$ and S $2p_{3/2}$) and a sulfate peak. The XPS peaks at binding energy of 161.9 and 163.0 eV are attributed to the S^{2-} $2p_{1/2}$ and S^{2-} $2p_{3/2}$ of MoS₂ while the small peak at 168.7 eV can be due to the partial oxidation of the sulfide. Moreover, the XPS spectra of the Ni 2p and Co 2p confirms the doping of Ni and Co in the MoNiS and MoCoS catalysts. In the Ni 2p spectrum, the peaks at 853.1 and 870.4 eV belong to Ni^{2+} , while the peaks at 856.4 and 874.1 eV belong to Ni^{3+} , indicating the coexistence of Ni^{2+} and Ni^{3+} in MoNiS. Multivalent Co^{2+} and Co^{3+} in MoCoS are also observed according to the XPS peaks indexed to Co^{3+} at 778.8 and 794.0 eV and to Co^{2+} at 781.5 and 797.5 eV . These results agree well with the reported Ni or Co doped MoS₂ materials [16,24,25]. The surface elemental contents in atomic percentage from the XPS analysis are listed in Table S1. Note that the small deviation of atomic ratios for the MoNiS and MoCoS from XPS study compared to the EDX results could be attributed to slightly more exposure of Mo atoms onto the surface of the sulfides relative to the S atoms.

3.2. Individual HDS and HDN

The catalytic activity of c-MoS₂, MoS₂, MoNiS, and MoCoS for the HDS and HDN is first evaluated individually in a batch reactor using thiophene and pyridine as the sulfur- and nitrogen-containing compounds. In the HDS reaction, the volume ratio of thiophene, tetralin and hexane is set to 1:9:10, whereas the volume ratio of pyridine, tetralin and hexane is set to 0.4:9:10.6 for the HDN reaction. Such reactant mixtures give relatively high sulfur and nitrogen contents in percentage levels, which are close to that of crude oils [33]. The reactor is initially pressurized with hydrogen gas to 11 bar and heated up to 300°C for different times. Fig. 6a shows the thiophene conversion after the HDS without catalyst and with c-MoS₂, MoS₂, MoNiS, and MoCoS at different time points. The blank test for 5 h gives a very low conversion of 1%, suggesting the high thermal stability of thiophene, whereas a conversion of 23% is obtained by the c-MoS₂. When MoS₂ are introduced in the HDS reaction, thiophene conversion is significantly enhanced and the conversion increases along with the reaction time. After reaction for 5 h, a thiophene conversion of 64% is achieved. The strong activity enhancement compared to the multilayer c-MoS₂ should be attributed to the much higher density of active edge sites of the ultrafine MoS₂ monolayers. When either MoNiS or MoCoS is employed as the catalyst, even higher thiophene conversions (above 80% after 5 h) are obtained compared to that of MoS₂, validating the promoting effect of the doped Ni and Co atoms. Nonetheless, the small conversion increment exhibited by MoCoS relative to that of MoNiS suggests that Co is a slightly better promoter than Ni in the HDS reaction. Assuming that the HDS of thiophene is a pseudo-first-order reaction, the residual thiophene concentration (i.e., 1-conv.) in logarithmic scale is linearly fitted with reaction time, as displayed in Fig. 6b. The line slope

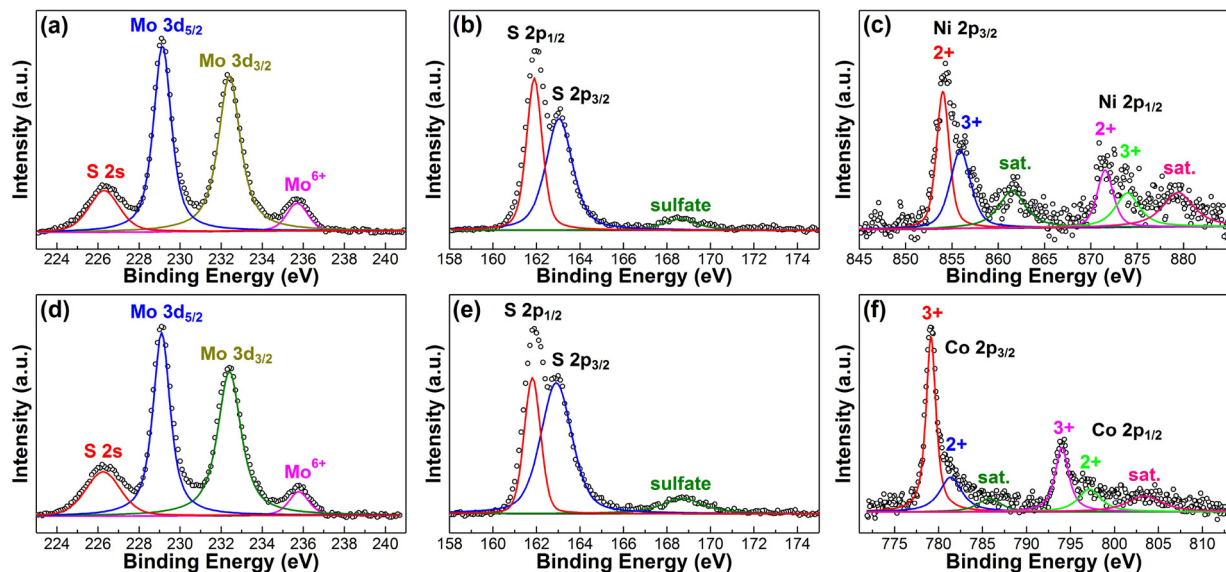


Fig. 5. High-resolution XPS spectra of Mo 3d (a), S 2p (b) and Ni 2p (c) regions of MoNiS, and Mo 3d (d), S 2p (e) and Co 2p (f) regions of MoCoS.

represents the reaction rate constant [10,24]. It can be seen that the HDS reaction kinetics is the fastest with the MoCoS catalyst compared to that with MoNiS and MoS₂.

The c-MoS₂, MoS₂, MoNiS, and MoCoS catalysts are further studied in the HDN of pyridine. Fig. 6c shows the pyridine conversion over the time course. The blank test indicates that pyridine is also thermally stable. The c-MoS₂ gives a relatively low pyridine conversion of 11% after 5 h. However, the conversion increases substantially in the presence of MoS₂, MoNiS or MoCoS. The difference of pyridine conversion among them is small and largely the same for the MoS₂ and MoCoS. MoNiS presents a slightly higher conversion compared with the other

two. This finding is also supported by the comparison of the reaction rate constants, as displayed in Fig. 6d. It is thus concluded that Ni is a more effective promoter than Co for the HDN reaction. Note that the thiophene conversion is much higher than the pyridine conversion although the initial thiophene concentration is even higher and the same reaction conditions are applied. This conversion difference manifests that the HDS reaction is more kinetically favorable than the HDN, considering the similar ring structure of thiophene and pyridine.

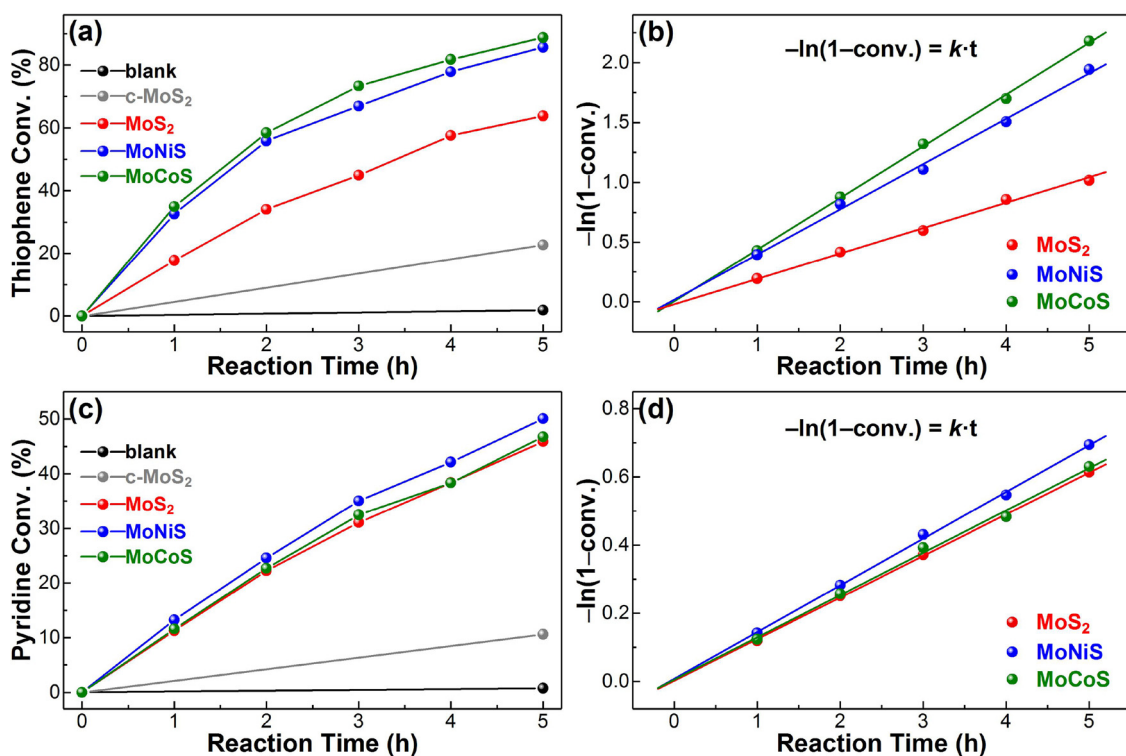


Fig. 6. (a) Thiophene conversion of the HDS reaction without catalyst and with c-MoS₂, MoS₂, MoNiS, and MoCoS for different times. (b) Corresponding kinetics of the HDS. (c) Pyridine conversion of the HDN reaction without catalyst and with c-MoS₂, MoS₂, MoNiS, and MoCoS for different times. (d) Corresponding kinetics of the HDN.

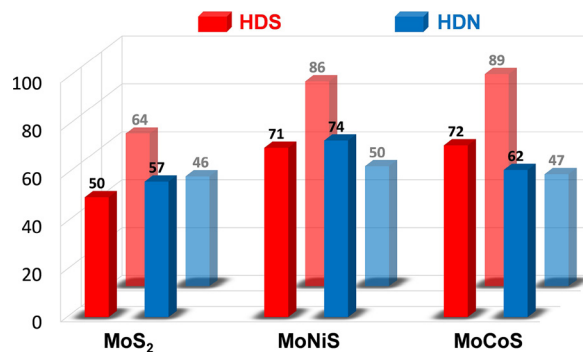


Fig. 7. Thiophene and pyridine conversions of the simultaneous (front row) and individual (back row) HDS and HDN reactions catalyzed by MoS₂, MoNiS and MoCoS for 5 h.

3.3. Simultaneous HDS and HDN

As a practical simulation of the hydrotreating conditions, we further investigate the catalytic activity of MoS₂, MoNiS and MoCoS in the simultaneous HDS and HDN by combining the model compounds. A solution consisting of thiophene, pyridine, tetralin, and hexane in the volume ratio of 0.5:0.2:9:10.3 is used as the feedstock. The reaction is held at 300 °C for 5 h. Fig. 7 presents the thiophene and pyridine conversion for the simultaneous and individual HDS and HDN catalyzed by MoS₂, MoNiS and MoCoS. The front row represents the simultaneous reaction, while the back row are data taken from the individual HDS and HDN in Fig. 6. It can be observed that for all the three catalysts, the thiophene conversions (red columns) are reduced in the simultaneous reaction in comparison with the individual HDS, whereas pyridine conversions (blue columns) increase obviously from the individual to the simultaneous reaction. The decreased HDS activity can be explained by the more favorable surface adsorption of pyridine molecules over the thiophene molecules onto the active sites of the catalysts when both of them are present in the reactant solution, demonstrating the potential role of nitrogen-containing compounds as a competitive inhibitor [40–42]. This finding is also supported by early theoretical density functional theory calculations, in which the authors demonstrate that the organonitrogen compounds bind more strongly than organosulfur compounds on certain sites of Ni- or Co-promoted MoS₂ [43,44]. Meanwhile, the increasing pyridine conversion should be attributed to its reduced concentration in the feedstock. Notably, MoNiS exhibits the best catalytic performance with both high thiophene and pyridine conversions of 71% and 74% compared to MoCoS and MoS₂.

3.4. Catalyst reusability

Catalyst reusability is an important factor to be considered for industrial applications. To this end, MoCoS and MoNiS, which show highest activity in the HDS and HDN, are tested in individual reaction for five consecutive cycles. Each reaction is held at 300 °C for 5 h. Fig. 8a shows the thiophene conversion of the HDS catalyzed by MoCoS and the pyridine conversion of the HDN catalyzed by MoNiS. No appreciable activity loss is observed for both catalysts after five cycles, indicating the remarkable reusability of the MoCoS and MoNiS monolayer catalysts. XRD patterns of the spent MoCoS and MoNiS catalysts after five cycles are compared with that of the fresh ones, as shown in Fig. 8b and c. It can be seen that the characteristic peak at 32.7°, corresponding to the (100) basal plane, is intensified after five runs for both the MoNiS and MoCoS catalysts, indicating the increasing in-plane crystallinity during the HDS and HDN reactions. However, no major (002) diffraction peaks are observed for both the spent catalysts, manifesting that no stacking along the c-axis occurs and the monolayer structure of MoNiS and MoCoS is well maintained throughout the tests. Furthermore, XPS analysis of the spent catalysts in Table S1 indicates that the surface elemental composition of MoNiS and MoCoS also remain unchanged. These results demonstrate the excellent structural stability of the MoNiS and MoCoS monolayers.

4. Conclusion

Monolayer MoS₂, MoNiS and MoCoS with similar ultrafine lateral sizes are successfully prepared via the organometallic decomposition method. OAm, which serves as both the solvent and surfactant, is inferred to play a critical role in the formation of monolayer structure and the control of lateral size of the MoS₂-based materials. Further comparative study using different solvent is required to offer precise strategy for size control. In the HDS and HDN reactions, these monolayer sulfides with high density of active sites exhibit significantly improved activity compared to the multilayer MoS₂. We also rationally confirm the better promoting role of Co than Ni in the HDS while the opposite in the HDN, and the competitive inhibition between the nitrogen- and sulfur-containing compounds in binding to active sites. Results presented in this work provide important insights in the understanding and design of future high-performance Mo-based catalysts for the HDS and HDN reactions in refineries.

Acknowledgements

The authors thank Prof. Vidar F. Hansen and Dr. Wakshum M. Tucho, University of Stavanger, for the TEM characterization. The authors also acknowledge the Research Council of Norway and the

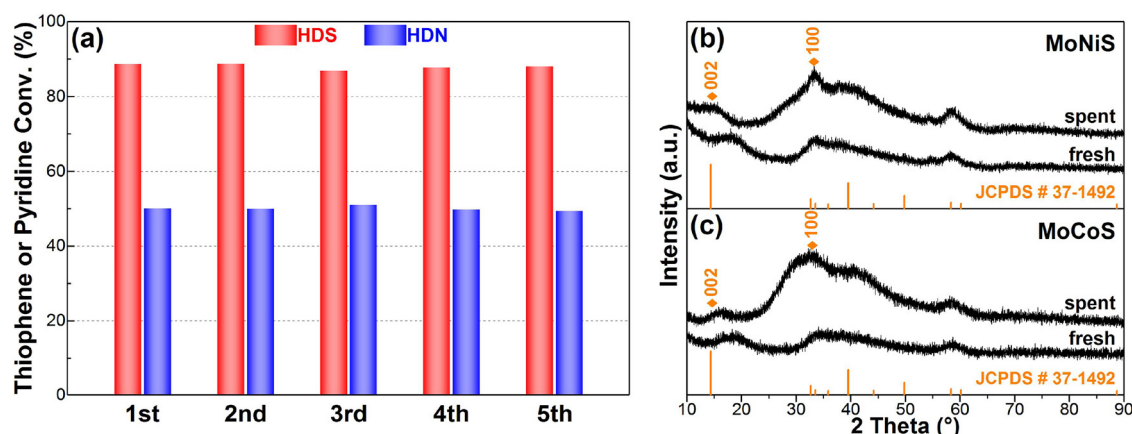


Fig. 8. (a) Thiophene and pyridine conversions for the HDS catalyzed by MoCoS and the HDN catalyzed by MoNiS for five consecutive cycles. XRD patterns of the fresh and spent MoNiS (b) and MoCoS (c) after five cycles.

industrial partners of The National IOR Centre of Norway for financial support.

Appendix A. Supplementary data

Supplementary material related to this article can be found, in the online version, at doi:<https://doi.org/10.1016/j.apcatb.2018.08.041>.

References

- [1] C. Song, X.L. Ma, *Appl. Catal. B-Environ.* 41 (2003) 207–238.
- [2] C.S. Song, *Catal. Today* 86 (2003) 211–263.
- [3] I.V. Babich, J.A. Moulijn, *Fuel* 82 (2003) 607–631.
- [4] G.H.C. Prado, Y. Rao, A. de Clerk, *Energy Fuels* 31 (2017) 14–36.
- [5] K. Guo, H. Li, Z. Yu, *Fuel* 185 (2016) 886–902.
- [6] H. Topsøe, *Appl. Catal. A: Gen.* 322 (2007) 3–8.
- [7] M. Breysse, B.A. Bennett, D. Chadwick, M. Vrinat, *Bull. Soc. Chim. Belg.* 90 (1981) 1271–1278.
- [8] R.R. Chianelli, *Catal. Rev.: Sci. Eng.* 26 (1984) 361–393.
- [9] R. Prins, V.H.J. De Beer, G.A. Somorjai, *Catal. Rev.: Sci. Eng.* 31 (1989) 1–41.
- [10] G. Liu, A.W. Robertson, M.M. Li, W.C.H. Kuo, M.T. Darby, M.H. Muhieddine, Y.C. Lin, K. Suenaga, M. Stamatakis, J.H. Warner, S.C.E. Tsang, *Nat. Chem.* 9 (2017) 810–816.
- [11] T. Tang, L. Zhang, W. Fu, Y. Ma, J. Xu, J. Jiang, G. Fang, F.S. Xiao, *J. Am. Chem. Soc.* 135 (2013) 11437–11440.
- [12] A.B. Laursen, S. Kegnaes, S. Dahl, I. Chorkendorff, *Energy Environ. Sci.* 5 (2012) 5577–5591.
- [13] D. Merki, X.L. Hu, *Energy Environ. Sci.* 4 (2011) 3878–3888.
- [14] Y. Li, H. Wang, L. Xie, Y. Liang, G. Hong, H. Dai, *J. Am. Chem. Soc.* 133 (2011) 7296–7299.
- [15] Q. Xiang, J. Yu, M. Jaroniec, *J. Am. Chem. Soc.* 134 (2012) 6575–6578.
- [16] H.T. Wang, C. Tsai, D.S. Kong, K.R. Chan, F. Abild-Pedersen, J. Norskov, Y. Cui, *Nano Res.* 8 (2015) 566–575.
- [17] J. Kibsgaard, Z. Chen, B.N. Reinecke, T.F. Jaramillo, *Nat. Mater.* 11 (2012) 963–969.
- [18] H. Li, C. Tsai, A.L. Koh, L. Cai, A.W. Contryman, A.H. Fragapane, J. Zhao, H.S. Han, H.C. Manoharan, F. Abild-Pedersen, J.K. Norskov, X. Zheng, *Nat. Mater.* 15 (2016) 48–53.
- [19] Y. Yan, B. Xia, X. Ge, Z. Liu, J.Y. Wang, X. Wang, *ACS Appl. Mater. Interfaces* 5 (2013) 12794–12798.
- [20] P. Afanasiev, G.F. Xia, G. Berhault, B. Jouguet, M. Lacroix, *Chem. Mater.* 11 (1999) 3216–3219.
- [21] Y. Zhao, L. Kuai, Y. Liu, P. Wang, H. Arandian, S. Cao, J. Zhang, F. Li, Q. Wang, B. Geng, H. Sun, *Sci. Rep.* 5 (2015) 8722.
- [22] P.P. Wang, H. Sun, Y. Ji, W. Li, X. Wang, *Adv. Mater.* 26 (2014) 964–969.
- [23] H. Hwang, H. Kim, J. Cho, *Nano Lett.* 11 (2011) 4826–4830.
- [24] W. Lai, Z. Chen, J. Zhu, L. Yang, J. Zheng, X. Yi, W. Fang, *Nanoscale* 8 (2016) 3823–3833.
- [25] J. Miao, F.X. Xiao, H.B. Yang, S.Y. Khoo, J. Chen, Z. Fan, Y.Y. Hsu, H.M. Chen, H. Zhang, B. Liu, *Sci. Adv.* 1 (2015) e1500259.
- [26] T.C. Ho, J.M. McConnachie, *J. Catal.* 277 (2011) 117–122.
- [27] Y.J. Yi, B.S. Zhang, X. Jin, L. Wang, C.T. Williams, G. Xiong, D.S. Su, C.H. Liang, *J. Mol. Catal. A-Chem.* 351 (2011) 120–127.
- [28] B. Yoosuk, J.H. Kim, C. Song, C. Ngamcharussrivichai, P. Prasassarakich, *Catal. Today* 130 (2008) 14–23.
- [29] B. Yoosuk, C.S. Song, J.H. Kim, C. Ngamcharussrivichai, P. Prasassarakich, *Catal. Today* 149 (2010) 52–61.
- [30] K.K. Liu, W. Zhang, Y.H. Lee, Y.C. Lin, M.T. Chang, C.Y. Su, C.S. Chang, H. Li, Y. Shi, H. Zhang, C.S. Lai, L.J. Li, *Nano Lett.* 12 (2012) 1538–1544.
- [31] M. Zhou, Z. Zhang, K. Huang, Z. Shi, R. Xie, W. Yang, *Nanoscale* 8 (2016) 15262–15272.
- [32] J.V. Lauritsen, J. Kibsgaard, S. Helveg, H. Topsøe, B.S. Clausen, E. Laegsgaard, F. Besenbacher, *Nat. Nanotechnol.* 2 (2007) 53–58.
- [33] K. Guo, V.F. Hansen, H.L. Li, Z.X. Yu, *Fuel* 211 (2018) 697–703.
- [34] K. Guo, H. Li, Z. Yu, *ACS Appl. Mater. Interfaces* 10 (2018) 517–525.
- [35] K. Guo, Y. Ding, J. Luo, Z. Yu, *ACS Appl. Mater. Interfaces* 10 (2018) 19673–19681.
- [36] M. Green, *Chem. Commun.* (2005) 3002–3011.
- [37] J. Lee, S. Zhang, S.H. Sun, *Chem. Mater.* 25 (2013) 1293–1304.
- [38] J. Deng, H. Li, S. Wang, D. Ding, M. Chen, C. Liu, Z. Tian, K.S. Novoselov, C. Ma, D. Deng, X. Bao, *Nat. Commun.* 8 (2017) 14430.
- [39] R. Ganatra, Q. Zhang, *ACS Nano* 8 (2014) 4074–4099.
- [40] M. Egorova, R. Prins, *J. Catal.* 241 (2006) 162–172.
- [41] T.C. Ho, L. Qiao, *J. Catal.* 269 (2010) 291–301.
- [42] T.A. Zepeda, B. Pawelec, R. Obeso-Estrella, J.N.D. de Leon, S. Fuentes, G. Alonso-Nunez, J.L.G. Fierro, *Appl. Catal. B-Environ.* 180 (2016) 569–579.
- [43] S. Rangarajan, M. Mavrikakis, *ACS Catal.* 7 (2016) 501–509.
- [44] S. Rangarajan, M. Mavrikakis, *ACS Catal.* 6 (2016) 2904–2917.